Experimental Evaluation of Inlet Distortion on an Ejector Powered Hybrid Wing Body at Take-off and Landing Conditions

Melissa B. Carter*, Patrick R. Shea,† and Jeffrey D. Flamm‡
NASA Langley Research Center, Hampton, VA 23681, USA

Michael Schuh§ and Kevin D. James¶
NASA Ames Research Center, Moffett Field, CA 94035, USA

Matthew R. Sexton,‖ Daniel M. Tompkins,** and Michael D. Beyar††
The Boeing Company, Huntington Beach, CA 92647, USA

As part of the NASA Environmentally Responsible Aircraft project, an ultra high bypass ratio engine integration on a hybrid wing body demonstration was planned. The goal was to include engine and airframe integration concepts that reduced fuel consumption by at least 50% while still reducing noise 42 db cumulative on the ground. Since the engines would be mounted on the upper surface of the aft body of the aircraft, the inlets may be susceptible to vortex ingestion from the wing leading edge at high angles of attack and sideslip, and separated wing/body flow. Consequently, experimental and computational studies were conducted to collect flow surveys useful for characterizing engine operability. The wind tunnel tests were conducted at two NASA facilities, the 14- by 22-foot at NASA Langley and the 40- by 80-foot at NASA Ames Research Center. The test results included in this paper show that the distortion and pressure recovery levels were acceptable for engine operability. The CFD studies conducted to compare to experimental data showed excellent agreement for the angle of attacks examined, although failed to match the low speed experimental data at high sideslip angles.

Nomenclature

AEDC	Arnold Engineering Development Center
AIP	Aerodynamic Interface Plane
ARC	Ames Research Center
BR&T	Boeing Research and Technology
DPCP_i	Average SAE circumferential distortion for ring i, $(\Delta PC/P)$
DPCP_{avg}	Rake average SAE circumferential distortion $(\Delta PC/P)$
ERA	Environmentally Responsible Aircraft
HWB	Hybrid wing body
LaRC	Langley Research Center

*Aerospace Engineer, Configuration Aerodynamics Branch, Mail Stop 499, AIAA Senior Member.
†Aerospace Engineer, Configuration Aerodynamics Branch, Mail Stop 499, AIAA Member.
‡Aerospace Engineer, Configuration Aerodynamics Branch, Mail Stop 499, AIAA Associate Fellow.
§Aerospace Engineer, System Analysis Office, Mail Stop 258-1.
¶Aerospace Engineer, Experimental Aero-Physics Branch, Mail Stop 260-1, AIAA Associate Fellow.
‖AIAA Member.
**Propulsion Engineer, Boeing Research & Technology, 14900 Bolsa Chica Rd., AIAA Senior Member.
††Aerodynamics Engineer, Boeing Research & Technology, 14900 Bolsa Chica Rd., AIAA Member.

NFAC	National Full-Scale Aerodynamics Complex
θi	Angular limits of integration
θ	Angular extent of *PAVLOW*
θ^+	Angular extent of positive swirl angle
θ^-	Angular extent of negative swirl angle
PAVLOW	Average total pressure ratio of low total pressure region for ring i
PAV	Average total pressure ratio for ring i
PR	Pressure ratio
Q	Dynamic pressure
R	Number of measurement rings
SA	Swirl angle
SI_i	Swirl intensity for ring i
SS^+	Positive sector swirl – average co-rotating swirl for a given measurement ring
SS^-	Negative sector swirl – average counter-rotating swirl for a given measurement ring
TPS	Turbine propulsion simulators
y^+	Nondimensional first cell height

I. Introduction

The NASA Aeronautics Research Mission Directorate mission is "to serve the future needs of aviation by conducting research into, and developing solutions for, the problems of flight."[1] In part to reach these goals, the Integrated Aviation Systems Program was created to focus on integrated, system-level, research that was flight oriented.[1] Within their projects, an ultra high bypass ratio engine integration on a hybrid wing body (HWB) demonstrator was planned as the centerpiece of the Environmentally Responsible Aircraft (ERA) project. The goal was to include engine and airframe integration concepts that reduced fuel consumption by at least 50% while still reducing noise by 42 dB cumulative on the ground.[2] Since the engines would be mounted on the upper surface of the aft body of the aircraft, the inlets may be susceptible to vortex ingestion from the wing leading edge at high angles of attack and sideslip and separated wing/body flow.

NASA, working with Boeing Research and Technology (BR&T), conducted a series of experimental and computational investigations on a twin-engine Boeing HWB configuration. Three experimental studies were planned to test a 5.75% wind tunnel model at low speeds. Each of the tests focused on a different simulation of the engines: flow-through nacelles, jet engine simulation ejectors, and turbine propulsion simulators (TPS). The flow-through nacelle test goal was to provide basic aerodynamic characteristics of the aircraft and select the best Krueger positions for takeoff and landing.[3] The ejector test used high pressure ejectors to represent realistic inflow conditions at the inlet of the engine. The TPS test used turbine engine simulators to accurately model the flow exiting the engine to determine the effect of jet exhaust on the control surfaces.[4] Computational studies were done to assist with the planning of these experimental studies[5] and to both compare with and add to the experimental database.

The ejector wind tunnel tests, the focus of this paper, were conducted to collect flow surveys useful for characterizing engine operability. This paper will briefly discuss the facilities and model used for this investigation along with the distortion and swirl parameters calculated and reported. A brief overview of the data uncertainty calculations as well as the computational methods used are also provided. Highlights from the experimental data are presented. Data consists of a comparison between computational results and experimental, i.e., wind tunnel, data.

II. Experimental Setup

Experimental work was performed at both the NASA Langley Research Center (LaRC) and the NASA Ames Research Center (ARC) in the 14- by 22-foot and 40- by 80-foot facilities, respectively. The following section outlines the experimental setup in both facilities and provides an overview of the model used.

II.A. NASA Langley 14- by 22-Foot Subsonic Wind Tunnel

The NASA Langley 14- by 22-foot subsonic wind tunnel facility is a closed return, atmospheric wind tunnel (Fig 1). The 50 ft long test section has a rectangular cross-section of 14.50 by 21.75 ft. The maximum

operating speed of the facility is 338 ft/sec, which corresponds to a unit Reynolds number of 2.15×10^6. A detailed description of the facility can be found in the work by Gentry et al.[6] For the current study, the tunnel was operated at dynamic pressures, Q, of 3.7, 6.2, 14.8, 33.3, and 59.2 psf, which correspond to approximate Mach numbers of 0.050, 0.065, 0.100, 0.150, and 0.200, respectively. The hybrid wing body test model (detailed in Section II.II.C) was mounted on a continuously adjustable sting system with three degrees of freedom (pitch, plunge, and yaw) that held the test model centered in the test section for the range of desired angle of attacks (-4 to 30°) and sideslip angles (±45°). The high pressure air required

Figure 1: NASA Langley's 14- by 22-foot wind tunnel.

for operating the ejectors (detailed in Section II.II.C) was supplied through the NASA Langley field wide high pressure air supply system. The flow was regulated down to the desired model supply pressure then fed to the model via 2 flexible stainless steel high pressure tubes. At the model, a pressure switch acted as the model safety system preventing accidental overpressurization and a separate transducer was used for recording the pressure level.

II.B. NASA Ames 40- by 80-Foot Subsonic Windtunnel

The National Full-Scale Aerodynamics Complex (NFAC) at NASA Ames is managed and operated by the Air Force Arnold Engineering Development Center (AEDC). The complex contains two test sections, the 40- by 80-foot test section (Fig 2) and the 80- by 120-foot test section. While both test sections are subsonic and atmospheric, the 40- by 80-foot tunnel is a closed return while the 80- by 120-foot is an open return. Figure 3 shows the circuit diagram of the NFAC and how the air flow is directed depending on the test section that is currently operating.

Figure 2: NASA Ames's National Full-Scale Aerrodynamics Complex (NFAC).

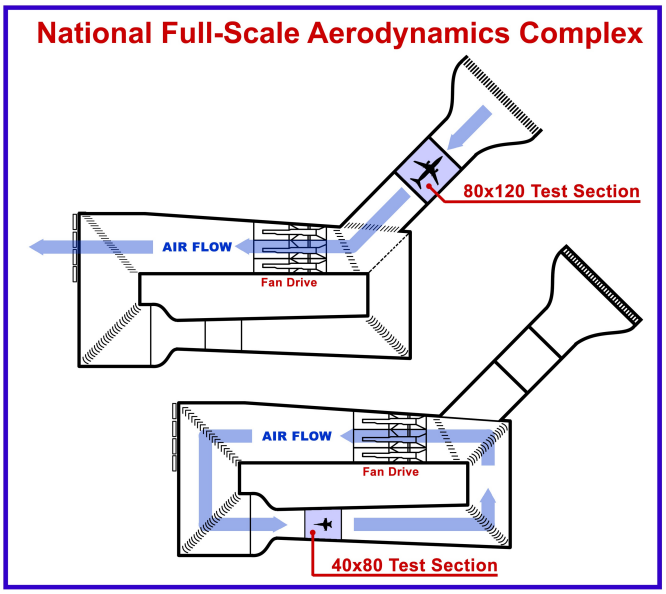

Figure 3: Circuit diagram of the NFAC including the 40- by 80-foot and 80- by 120-foot test sections.

All of the HWB testing conducted at NFAC was in the 40- by 80-foot test section. The test section has semi-circular sides with a 19.5-foot radius and the overall dimensions are 39 by 79 by 80 ft. The maximum operating speed of the facility is 506 ft/sec, which corresponds to a Reynolds number per foot of 3.0×10^6. A detailed description of the facility can be found in references 7 and 8. As was done at 14- by 22-foot, the tunnel was operated at dynamic pressures, Q, of 3.7, 6.2, 14.8, 33.3, and 59.2 psf that correspond to approximate Mach numbers of 0.050, 0.065, 0.100, 0.150, and 0.200, respectively. Unlike the 14- by 22-foot, the sting support system at 40- by 80-foot is at a constant height and therefore did not hold the model centered in the test section. The sting support system still provided two degrees of freedom and the testing included angles of attack of -5 to 28° and sideslip angles of ±45°.

The high pressure air required for operating the ejectors (detailed in Section II.II.C) was supplied through the NASA Ames high pressure air system. The flow was regulated down to the desired model supply pressure then fed to the model via 2 flexible stainless steel high pressure tubes. Under the tunnel test section, rupture disks were used as the model safety system preventing accidental over pressurization and separate transducers located at the ejectors were used for recording the pressure level.

II.C. Hybrid Wing Body Model

A 5.75% scale HWB model designed as ERA HWB-0009GM was fabricated for testing.[9] The model was made to accommodate three different testing goals: general performance and stability and control using flow through nacelles or no engines, flow distortion using ejectors, and stability and control using turbine powered simulator units. Additionally, the model had an optional Krueger with numerous settings, detachable vertical tails with ruddervators and 9 deflectable elevons. Some model dimensions are listed in table 1; additional information on the model can be found in references 3 or 9.

Table 1: HWB Model Dimensions.

Model span	13.187 ft
Model length	6.95 ft
Mean aerodynamic chord	3.717 ft

For the purposes of this experimental investigation, two Krueger settings were tested, vertical tails attached and all elevons and ruddervators set at zero-degrees deflection. This paper will only present data for one Krueger position: 45°, 3,2.[10] The model as installed in the 14- by 22-foot tunnel is shown in figure 4.

Two jet engine simulation ejectors were used to simulate the expected inlet mass flow conditions. The TDI model 1900A ejectors operate by blowing high pressure air through multiple nozzles located inside a

canister mounted downstream of the nacelle inlet. The nozzle flow entrains air drawn though the nacelle inlet. By varying the supply air pressure to the ejector, the air mass flow drawn through the inlet can be adjusted. The ejectors were mounted to long nacelles and attached directly to the model sting support system. Pylons were located near the front of the nacelles and cantilevered over the surface of the model with foam seals in between the pylon and the model. Figure 5 shows a 3/4 rear view of the model with the long nacelles and the ejectors attached at the exhaust.

A distortion rake and a swirl rake were mounted at the front of the left- and right-hand nacelles, respectively. They were located at the aerodynamic interface plane (AIP), which is shown in figure 6. The distortion rake contained 40 total pressure probes (Fig 7b). The swirl rake consisted of three arms with five 5-hole probes each as shown in figure 7a. The 5-hole probes were calibrated prior to installation so that flow angularity could be calculated as a function of the pressure readings. The swirl rake obtained data at 15-degree increments. The area weighted probe distribution for the distortion and swirl rakes (when the swirl rake was rotated in 15-degree increments) is shown in figure 8. Just in front of the ejectors in each nacelle was a 40 probe rake to measure inlet mass flow. One pressure probe on each rake was replaced with a thermocouple to measure the temperature of the flow. These measurements were used to set the desired mass flow rates to the approximate desired engine power settings. Figure 6 shows a center cut of one of the nacelles and ejector that labels the parts described above.

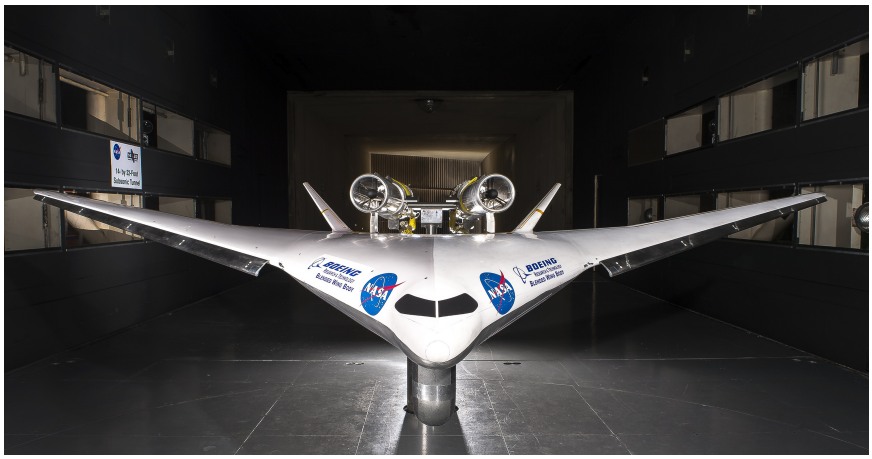

Figure 4: HWB model with ejectors in 14- by 22-foot test section.

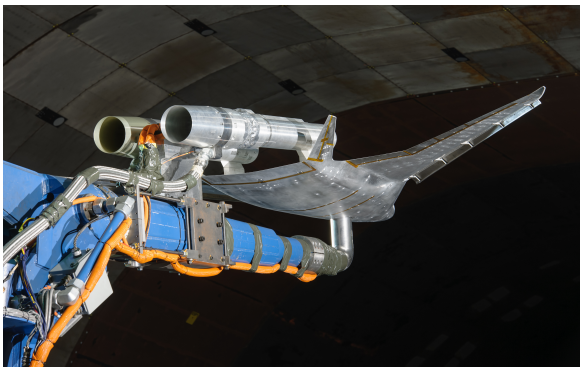

Figure 5: HWB model with ejector powered inlets installed in 40- by 80-foot test section.

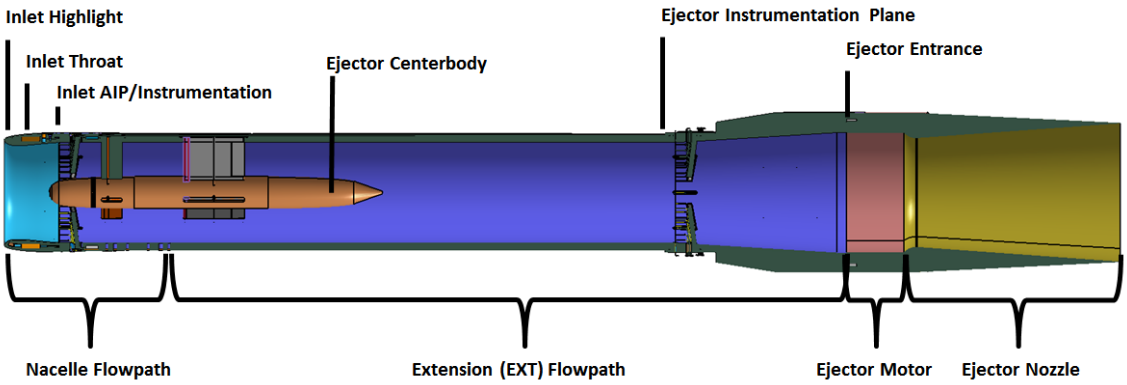

Figure 6: Center cut of the nacelle and ejector.

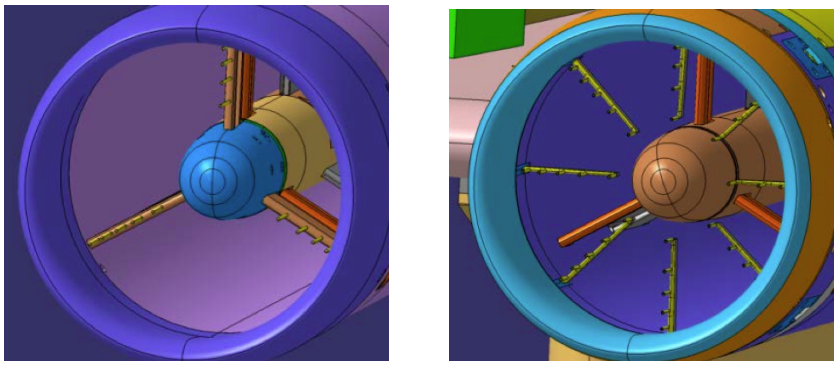

(a) Swirl rake (right inlet) (b) 40 probe rake (left inlet)

Figure 7: Close-up view of pressure rakes within the inlets (looking downstream).

(a) Swirl rake (right inlet) (b) 40 probe rake (left inlet)

Figure 8: Pressure rake area weighted probe distribution (looking downstream).

III. Theoretical Background

III.A. Inlet Pressure Recovery (PR)

An inlet's performance is characterized by the inlet total pressure recovery. This is a measurement of the amount of the flow into the inlet that matches free stream flow conditions and calculated using equation 1 below.

$$PR_{avg} = average(PR) \; where \; PR = \frac{PT}{PT_{inf}} \tag{1}$$

For subsonic flight, a typical inlet has a pressure recovery of 0.98 or better while values below 0.96 could significantly impact engine performance.[11]

III.B. Inlet Distortion Intensity (DPCP)

Another method of characterizing inlet performance is the distortion intensity (DPCP or $\Delta PC/P$). The basic concept for calculating the distortion intensity is depicted in Figure 9 where the distortion intensity is calculated as the area identified in gray divided by the angular extent of the area (a detailed description of these calculations can be found in the SAE Report AIR1419).[12] Note that the area indicated in gray is

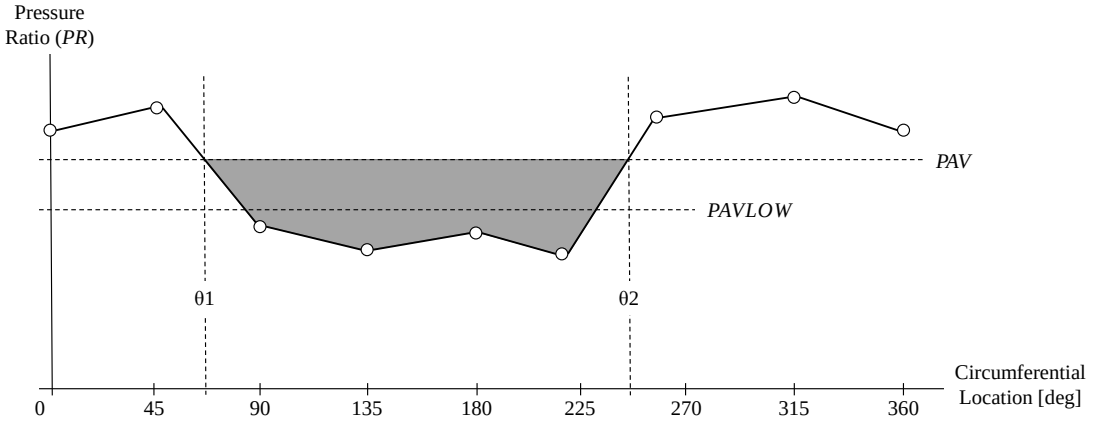

Figure 9: Example dataset and nomenclature used for DPCP calculations (adapted from SAE Report AIR1419[12]).

defined by the measurement locations that have a pressure ratio (PR) below the average ring pressure ratio (PAV). Using the nomenclature defined in Figure 9, $PAVLOW$ is calculated as

$$PAVLOW = \frac{1}{\theta} \int_{\theta 1}^{\theta 2} (PR)\, d\theta \tag{2}$$

where the integral is computed discretely due to the finite number of measurement locations. The angular extent of the area, θ, is calculated as

$$\theta = \theta 2 - \theta 1 \tag{3}$$

and the average pressure ratio for a measurement ring (PAV) is calculated as

$$PAV = \frac{1}{360} \int_{0}^{360} (PR)\, d\theta \tag{4}$$

where the integral is again computed discretely due to the finite number of measurement locations. DPCP for a given ring (ring number represented as a subscript i) is calculated by normalizing $PAVLOW$ by PAV (equation 5).

$$DPCP_i = \frac{PAV_i - PAVLOW_i}{PAV_i} \tag{5}$$

The total DPCP for a measurement plane is calculated by taking the mean of the DPCP ring values (equation 6) where R is the number of measurement rings.

$$DPCP_{avg} = \frac{1}{R} \sum_{i=1}^{R} DPCP_i \tag{6}$$

Acceptable levels for DPCP are generally below 0.05 for commercial aircraft.[13]

III.C. Inlet Swirl Intensity

The inlet swirl intensity provides a measure of the flow angularity at the aerodynamic interface plane. Figure 10 provides an example one-per-revolution swirl distribution and the corresponding nomenclature that will be used to describe the calculations. A detailed description of swirl and the corresponding calculations can be found in the SAE Report AIR5686.[14] The first step in calculating the swirl intensity is to separate

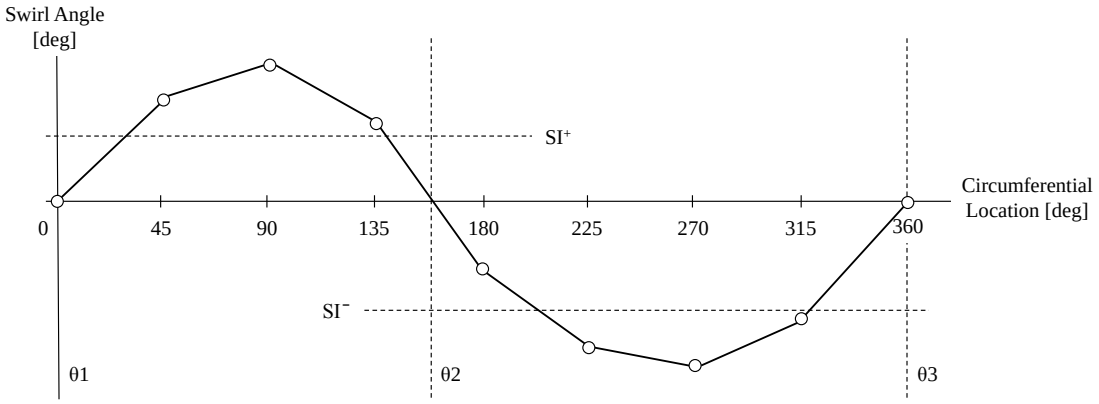

Figure 10: Example dataset and nomenclature used for circumferential swirl calculations (adapted from SAE Report AIR5686[14]).

the regions of positive and negative swirl along the measurement ring. The angular extent of these regions (θ^+ and θ^-, respectively) are calculated as seen in equations 7 & 8.

$$\theta^+ = \theta 2 - \theta 1 \tag{7}$$

$$\theta^- = \theta 3 - \theta 2 \tag{8}$$

The sector swirl is calculated as the average swirl angle for a given angular extent as seen in equations 9 & 10.

$$SS^+ = \frac{1}{\theta^+} \int_{\theta 1}^{\theta 2} (SA)\, d\theta \tag{9}$$

$$SS^- = \frac{1}{\theta^-} \int_{\theta 2}^{\theta 3} (SA)\, d\theta \tag{10}$$

Similar to the calculations of *PAVLOW* and *PAV*, the integrations for SS^+ and SS^- are computed discreetly due to the finite number of measurement locations. The overall swirl intensity for a measurement ring (SI_i) is calculated as seen in equation 11 where the magnitude of SS^+ and SS^- are the values of interest. SS^- will have a negative value by definition and therefore the absolute value of SS^- is used for the calculation of *SI*.

$$SI_i = \frac{(SS^+)\,(\theta^+) + (|SS^-|)\,(\theta^-)}{360} \tag{11}$$

IV. Data Uncertainty

The pressure recovery uncertainties from the Langley 14- by 22-foot tests were calculated using a zeroth order approach based on the sensor resolutions. These uncertainties were propagated through the test equations using the methods outlined in Chapter 3 of the text by Taylor.[15] Time history data were provided for the data acquired at the NFAC 40- by 80-foot and these data were used to calculate a 95% confidence interval on the individual pressure signals, the average pressure recovery, and the derived DPCP values. The 95% confidence values were compared to the zeroth order calculations and the more conservative estimate selected.

A series of fifteen neural networks were trained to calculate the swirl angle directly from the 5-hole probe pressure data. As part of the training, a portion of the calibration data were reserved for use in

testing the neural network performance. Using the reserved test data, the neural network output was compared to the known calibration data and the 95% confidence intervals were defined based on the absolute difference between the known data (calibration) and predicted data (neural network output). The 95% confidence intervals for each of the fifteen 5-hole probes were then used to propagate through the swirl intensity derivations. More details on the uncertainty calculations and the neural network development can be found in the work by Carter et al.[10]

During the course of testing, several probes on the swirl rake were found to be reading incorrectly. For cases with missing probes, additional neural networks were trained to predict the swirl angle in the absence of the missing probes. That is, instead of training the neural network with five inputs (one pressure from each port of the 5-hole probe), the networks were trained with a subset of the inputs (as few as three inputs in some cases). When using all five inputs, the network confidence intervals were always found to be less than $\pm 0.45°$. However, when missing two probes, the confidence interval ranged from $\pm 5.65°$ to as high as $\pm 40.58°$ depending on the missing probe combinations.

V. Numerical Techniques

CFD studies were conducted to assist with the planning of the test and to compare results with experimental data. Tompkins, et al.[16] discusses the pre-test CFD work and some initial cases run to compare with experimental results. In addition to this work, two codes were used to simulate 6 experimental test conditions for direction comparisons. The two codes were STAR-CCM+ and CFD++.[17] For these simulations, STAR-CCM+ modeled the air as an ideal gas using the Reynolds-Averaged Navier-Stokes, k-omega SST (Menter) turbulence, and "All y^+" wall treatment models. Version 9.04.009 of the code was used to generate polyhedral meshes in free air with no modeling of the wind tunnel sting or walls and the first prism layer in the meshes was sized to have a wall y^+ value of 1 or less. CFD++ was run to obtain Reynolds Averaged Navier Stokes (RANS) solutions using unstructured grids which are comprised of a mixture of triangular prisms, tetrahedrals and pyramids. The grids were sized to have a y^+ value of less then 1. The primary turbulence model employed was the two-equation realizable k-epsilon model.

VI. Results

The results from the experimental and computational studies are presented in this section. Please note that all of the inlet plots are arranged such that the viewer is aft of the model and looking forward. Unless noted otherwise, all of the experimental results are from the swirl rake (RHS) at the 14- by 22-foot tunnel. Also as stated in section III, acceptable levels for PR are 0.96 or higher while DPCP is considered acceptable if lower then 0.05.

VI.A. Mass Flow Sweeps

The total pressure ratio plots, figure 11, indicate there is a small vortex that the engine may be ingesting as the mass flow reaches its maximum at Mach 0.05 and 0.1. However, for the Mach 0.065 case, the vortex appears at the lower mass flow rates. Although this vortex does not clearly appear in the higher mass flow rates, it may still exist and be located in between pressure probes. Figures 12 and 13 further show the effect of the vortex at the lower mass flow rates. The Mach 0.065 case has the lowest pressure recovery and highest DPCP average results for mass flow rates of 5.57 and 6.23 lbm/s. However, even with the small vortex present, the pressure recovery and average DPCP levels remain acceptable for all cases.

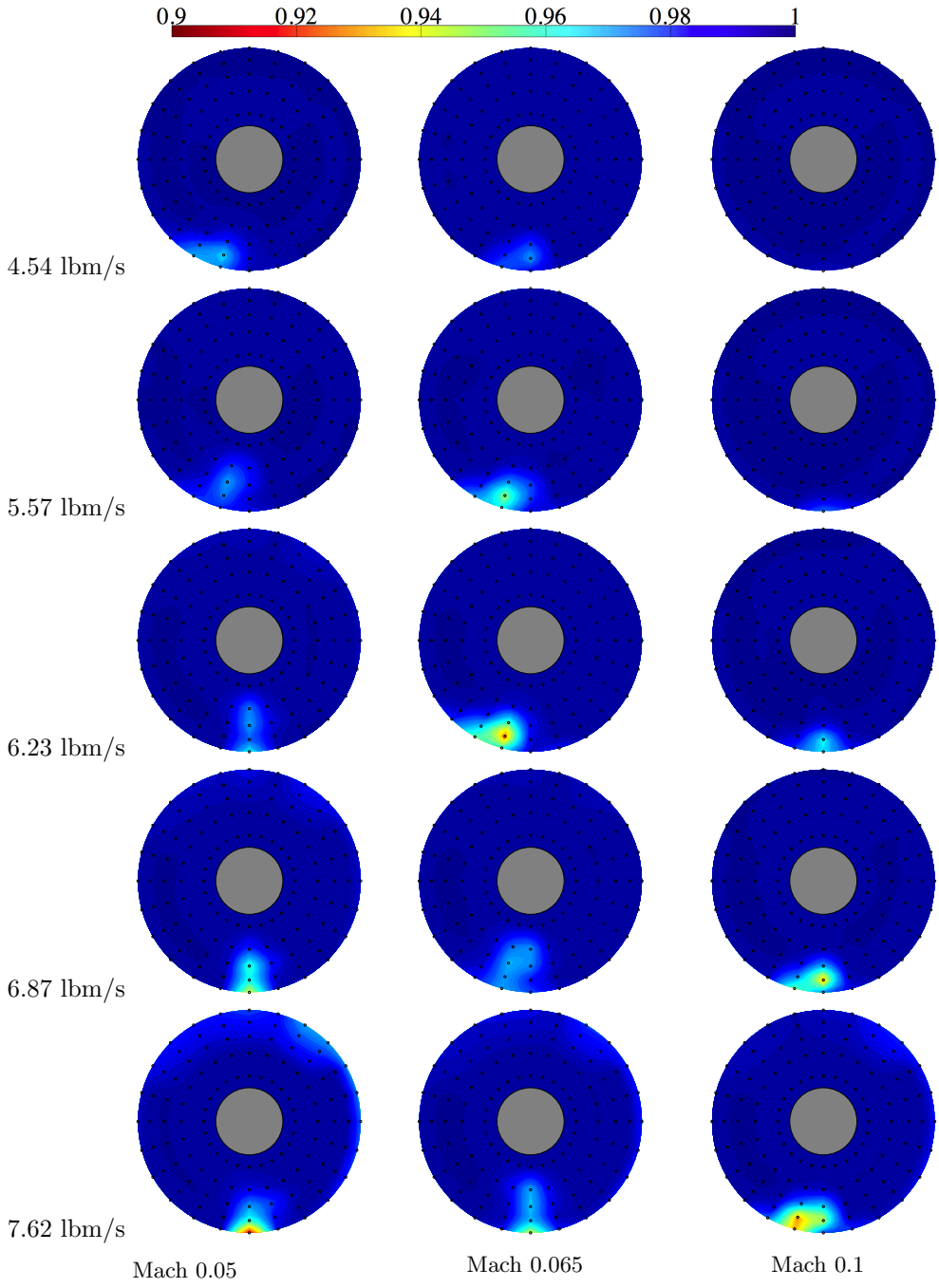

Figure 11: Effect of Mass flow rate on total pressure ratio at alpha 1°, beta 0°.

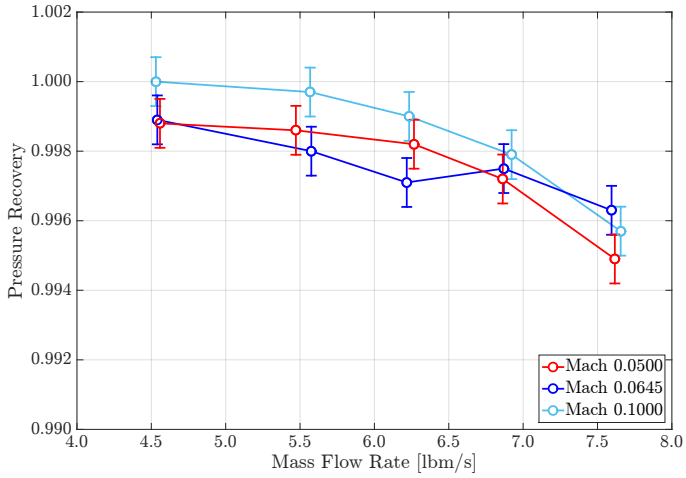

Figure 12: Pressure recovery versus mass flow rate, alpha 1°, beta 0°.

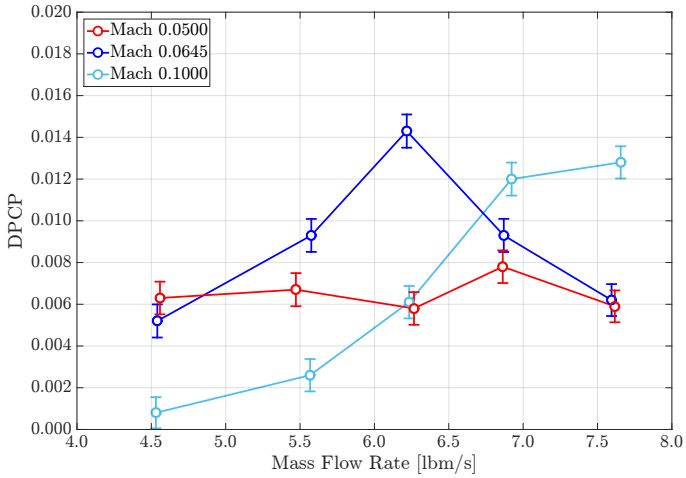

Figure 13: DPCP versus mass flow rate, alpha 1°, beta 0°.

VI.B. Compare CFD with Experimental Data

Two CFD codes, STAR-CCM+ and CFD++, were run to match 6 experimental data sets from the 14- by 22-foot wind tunnel. Data were then extracted at the same points that the pressure probes were located and run through the same data processing system used for the experimental results. Please note that the CFD++ results were only extracted for 40 probes instead of the 120 that was taken with the swirl rake. Consequently, the CFD++ data appears courser then the STAR-CCM+ and experimental data.

The first set of runs consisted of three angles of attack, -4°, 10° and 22°, at Mach 0.2 and a beta of 0°. These angles of attack produced very little distortion in the flow and the CFD does a good job of matching the results (Figs 14, 15, 16). The second set of runs consisted of three beta angles, 0°, -30° and -40°, at Mach 0.065 and an angle of attack of 1° (Figs 17, 18, 19). Although all of these cases indicated acceptable levels for pressure recovery and DPCP average, there was considerably more distortion in the flow when compared to the angle of attack sweep data. Both CFD codes did well predicting the beta 0° case but over predicted the flow distortion for the two larger beta angles. The CFD results predicted unacceptable distortion levels for the beta -40° case while the experimental data produced acceptable distortion levels.

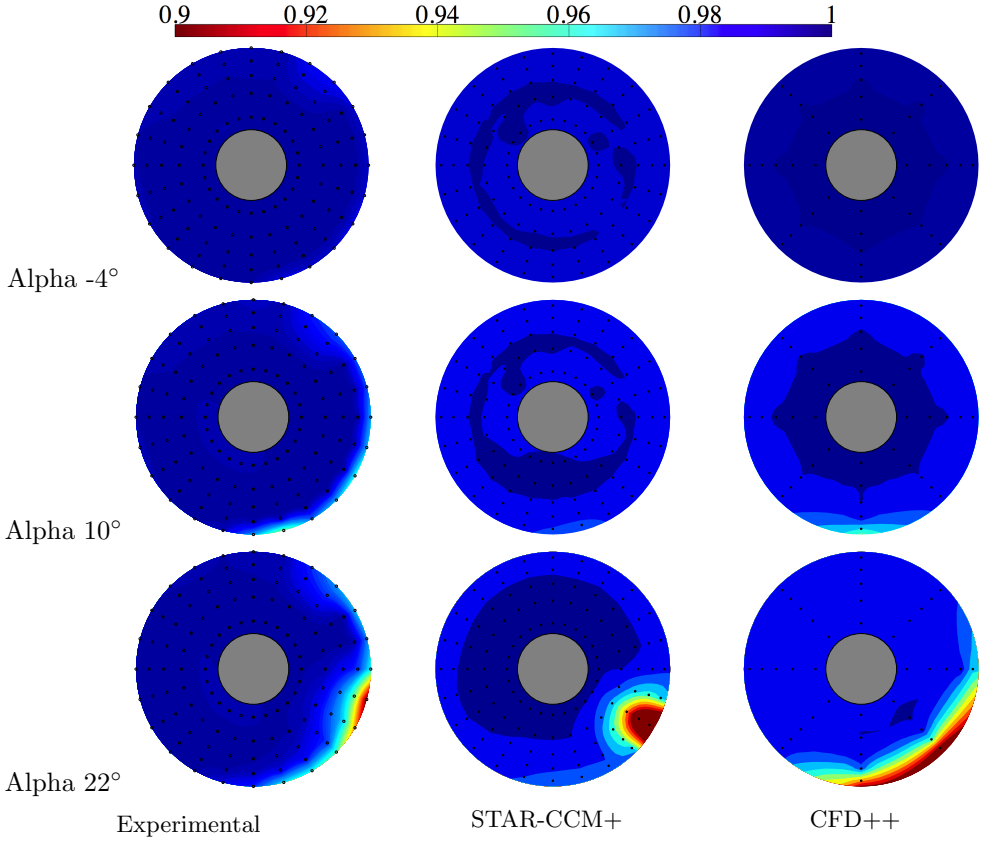

Figure 14: Total pressure ratio from experimental and computational methods at Mach 0.2, beta 0°.

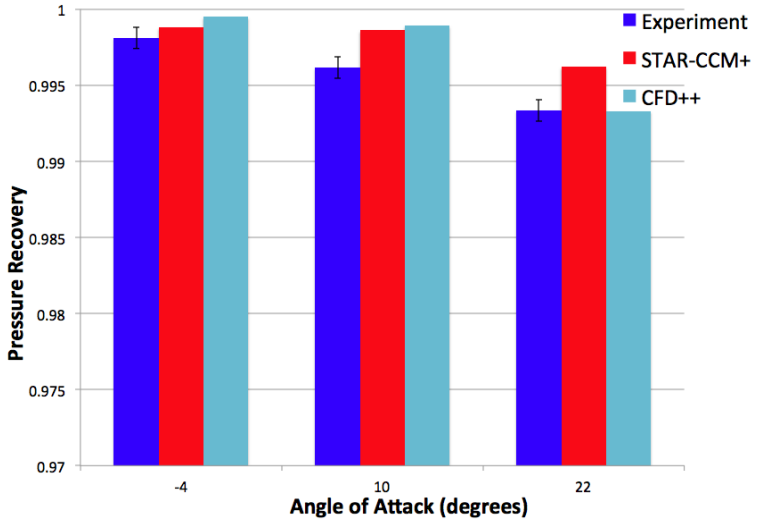

Figure 15: Pressure recovery versus alpha, Mach 0.2, beta 0°.

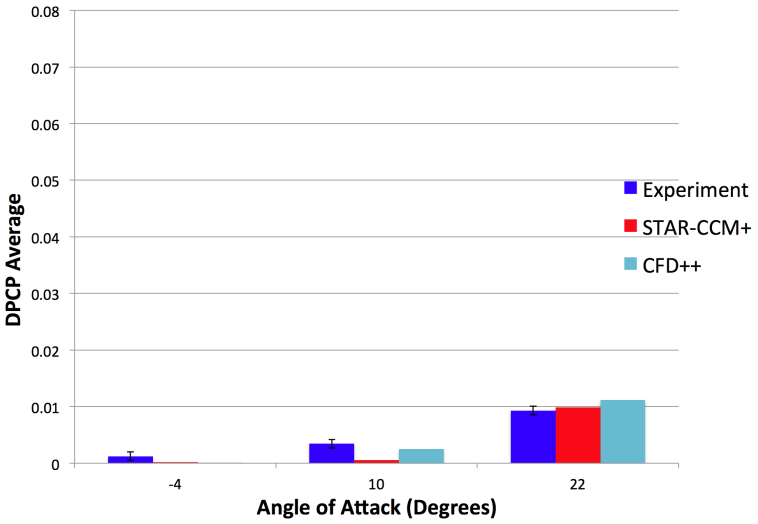

Figure 16: DPCP versus alpha, Mach 0.2, beta 0°.

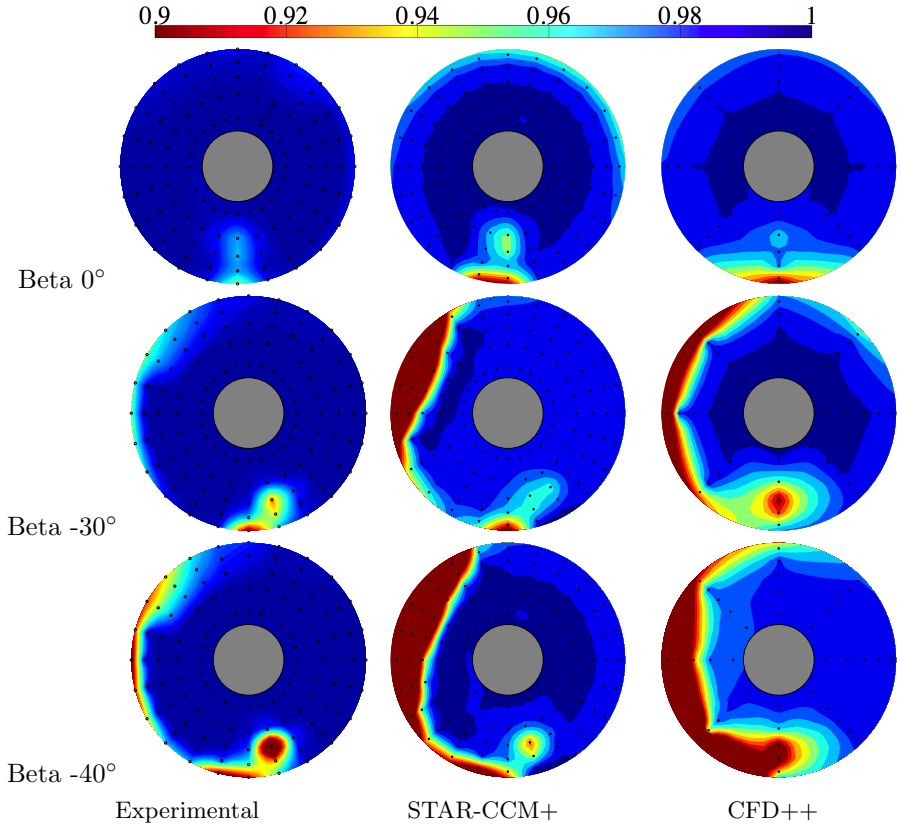

Figure 17: Total pressure ratio from experimental and computational methods at Mach 0.065, alpha 1°.

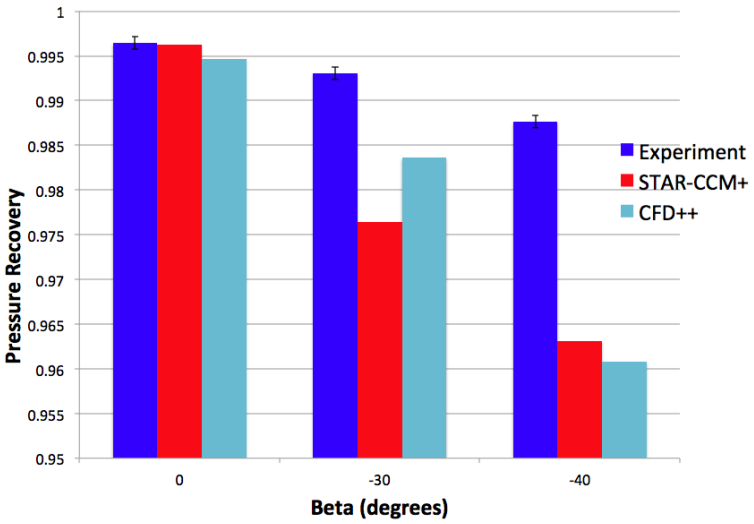

Figure 18: Pressure recovery versus beta, Mach 0.065, alpha 1°.

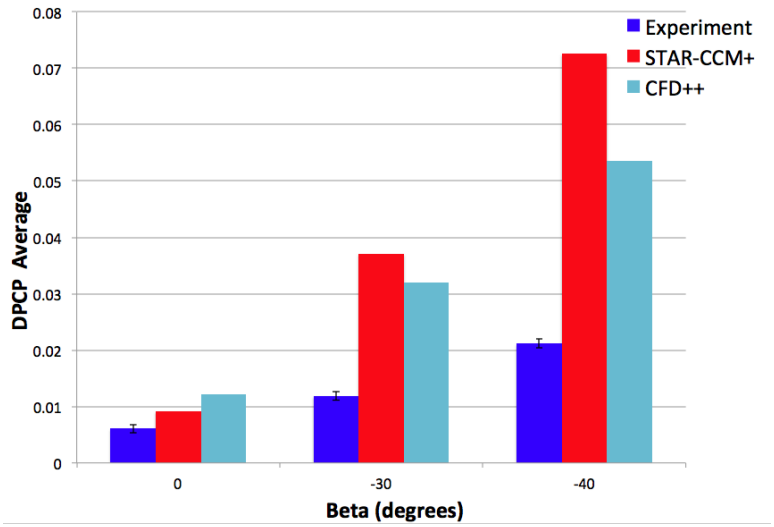

Figure 19: DPCP versus beta, Mach 0.065, alpha 1°.

VI.C. Wind Tunnel to Wind Tunnel Comparisons

Due to a motor issue with the 14- by 22-foot wind tunnel, testing was ended before all the desired data could be obtained. In order to ensure the success of this research program, testing was moved to 40- by 80-foot wind tunnel. Consequently, the situation presented the unique opportunity to compare tunnel to tunnel results. Figure 20 compares the total pressure ratio at the inlet of both nacelles in the two tunnels for two angles of attack. As can be seen, only minor differences exist. Figures 21 and 22 confirm this agreement numerically, with the majority of the results agreeing within the margin of uncertainty. Figures 23, 24 and 25 show slightly more disagreement, especially at the beta of -40° case. Considering that there are many factors that can contribute to slight discrepancies in the data, especially since testing was conducted in atmospheric tunnels so there are temperature and barometric pressure differences along with different tunnel flow qualities, these slight differences in results are more than acceptable.

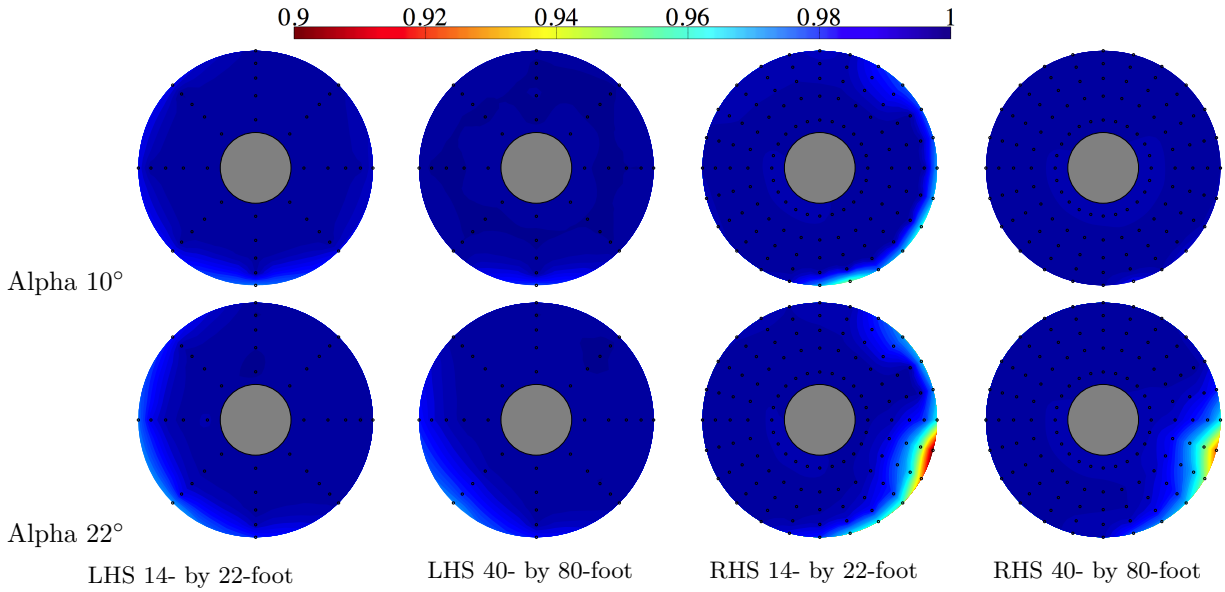

Figure 20: Total pressure ratio comparison from two tunnels at Mach 0.2, beta 0°.

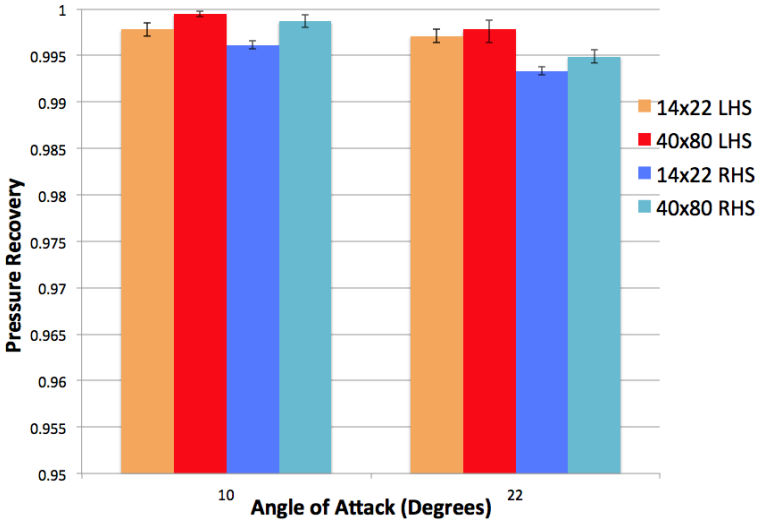

Figure 21: Pressure recovery versus alpha, Mach 0.2, beta 0°.

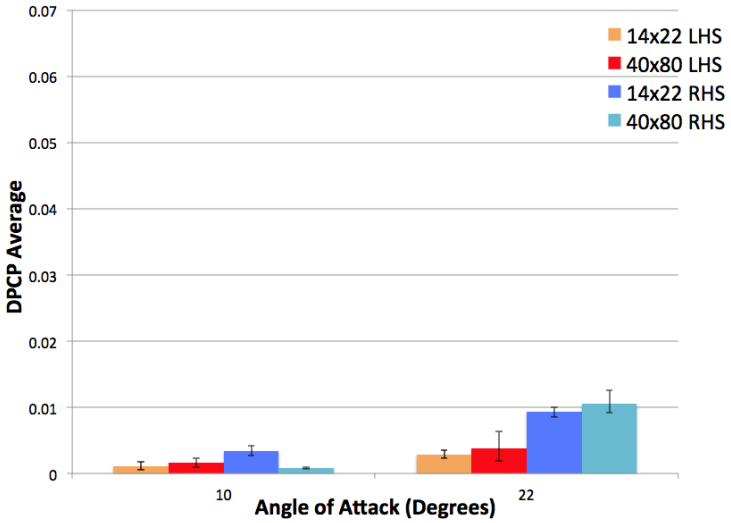

Figure 22: DPCP versus alpha, Mach 0.2, beta 0°.

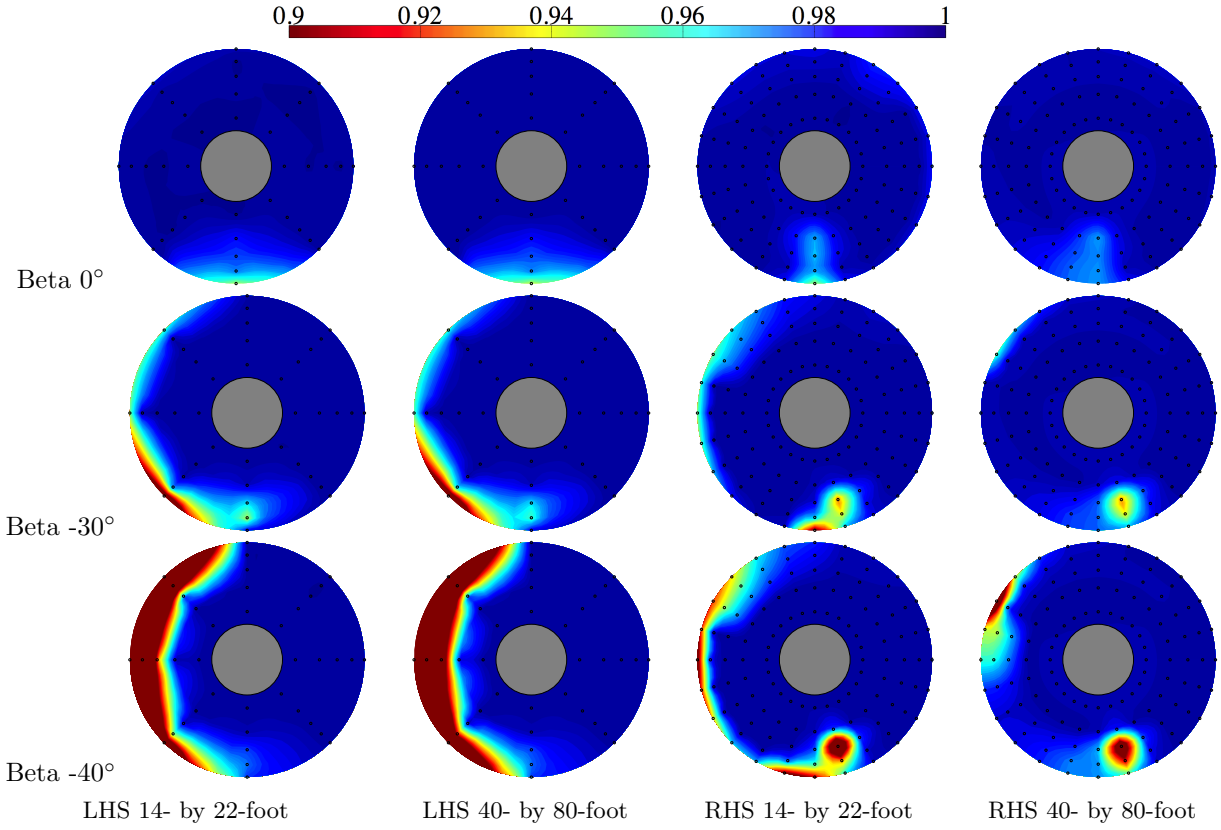

Figure 23: Total pressure ratio comparison from two tunnels at Mach 0.2, beta 0°.

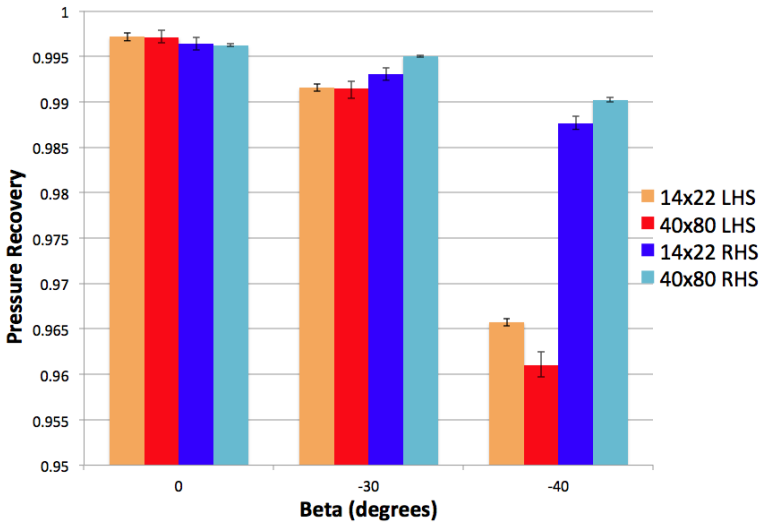

Figure 24: Pressure recovery versus beta, Mach 0.065, alpha 1°.

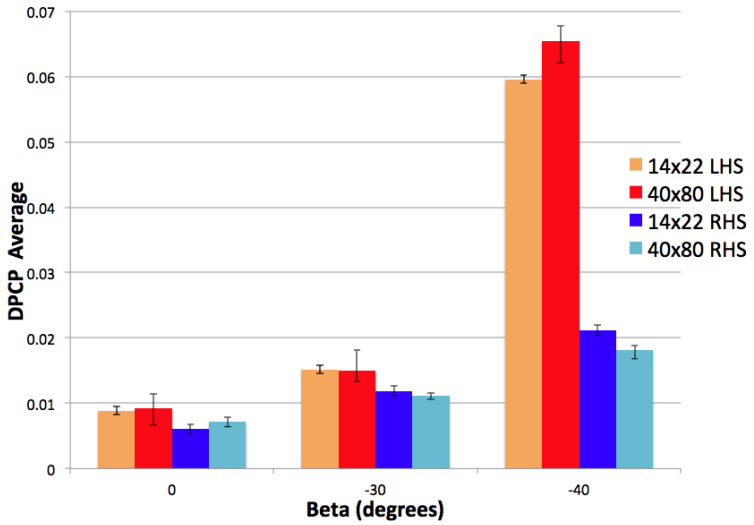

Figure 25: DPCP versus beta, Mach 0.065, alpha 1°.

VI.D. Swirl Characteristics

As discussed in sections II.II.C and III.III.C, swirl characteristics of the flow were obtained during the testing. Unfortunately, there is not a lot of published data that can be used to confirm acceptable levels of swirl.[14] Consequently, this section simply presents the swirl data for the same five cases presented in section VI.C and does not draw conclusions concerning its acceptability.

During testing, several of the pressure ports on the swirl rake failed. Although entries were made to repair as many as possible, there are data sets that contain missing pressure ports. It is for this reason that both tunnel sets of swirl data are shown so that it is easy to identify bad ports. If there is a bad port, it would affect 8 points within the data collection since the swirl rake was operated 8 times, at 15-degree increments, to obtain a data set. As can be seen in figure 26, the middle probe of the upper arm of the swirl rake had a failure (the yellow region). It was repaired prior to entry into 40- by 80-foot, so the 40- by 80-foot data shows that swirl angle remained small except in the lower right hand quadrant at an angle of attack of 22°. These results match what is seen for distortion in the previous section.

The beta cases are a little more challenging to distinguish the swirl characteristics. It appears there is a small vortex being ingested at the higher beta angles (fig 27). This vortex may be unsteady as there are slight differences between the results from the two tunnels both in the swirl angle and the pressure recovery plots in the previous section.

Figures 28 – 32 show the calculated swirl intensity and uncertainty for each of the 5 rings of pressure ports. Larger uncertainty bands are due to the failure of one (or two) of the probes in the 5-hole probe as discussed in section IV.

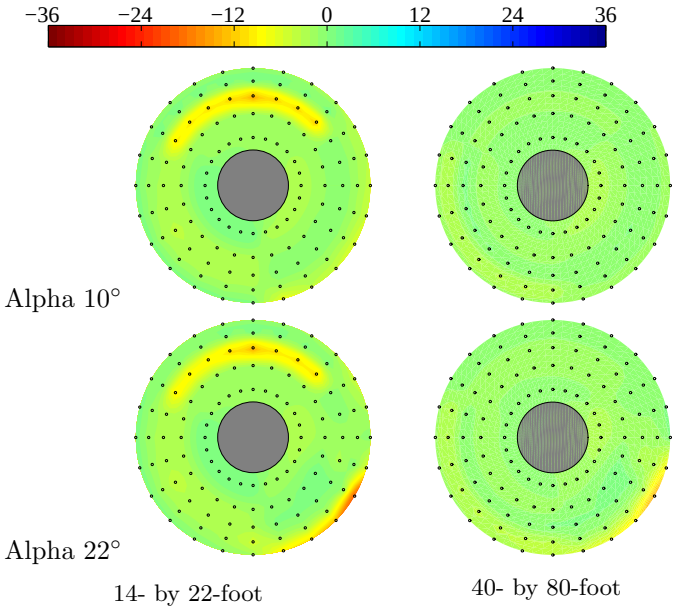

Figure 26: Swirl angle comparison from two tunnels at Mach 0.2, beta 0°.

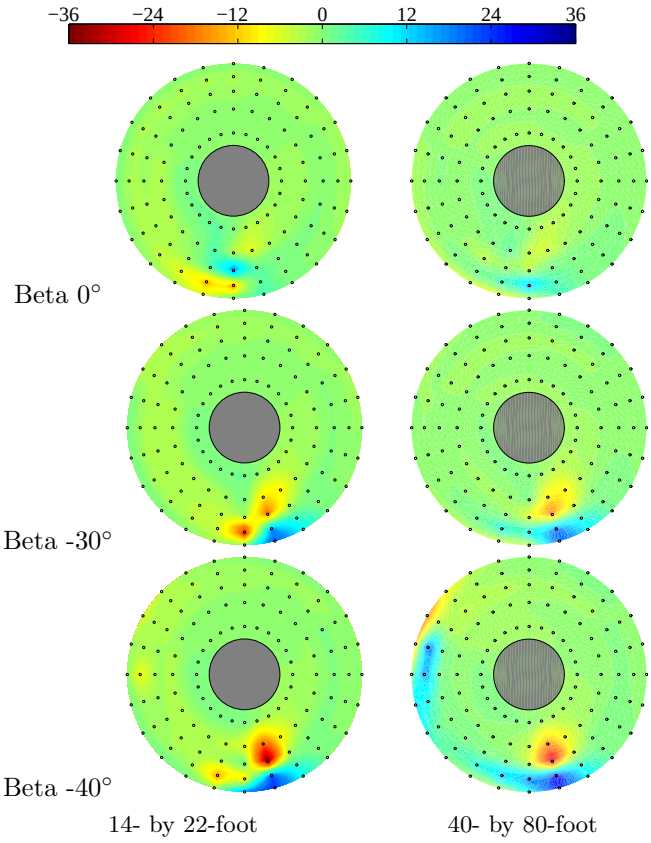

Figure 27: Swirl angle comparison from two tunnels at Mach 0.065, alpha 1°.

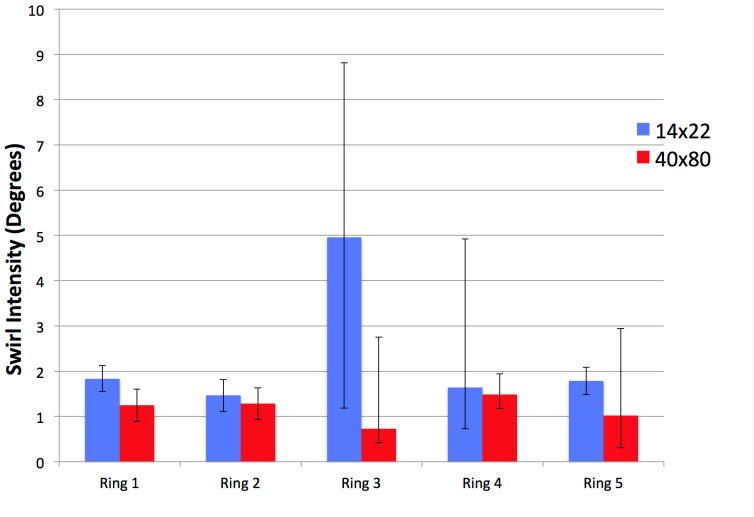

Figure 28: Swirl intensity alpha 10°, Mach 0.2, beta 0°.

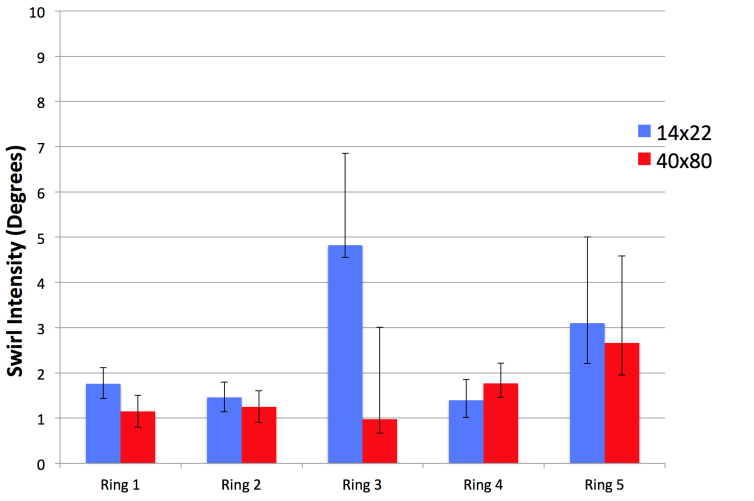

Figure 29: Swirl intensity alpha 22°, Mach 0.2, beta 0°.

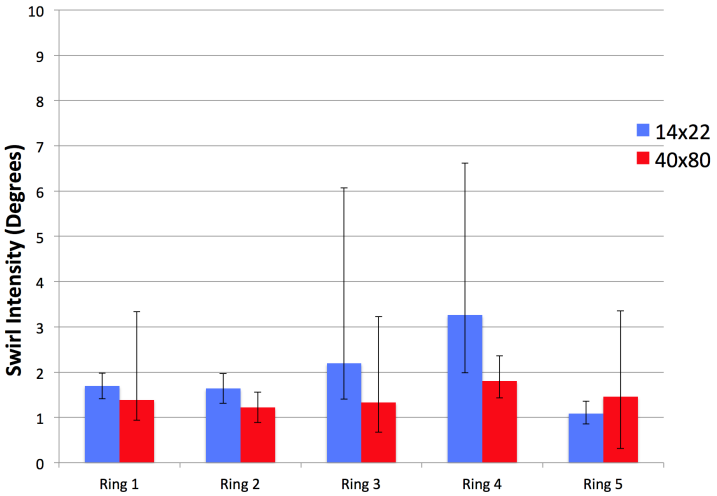

Figure 30: Swirl intensity beta 0°, Mach 0.065, alpha 1°.

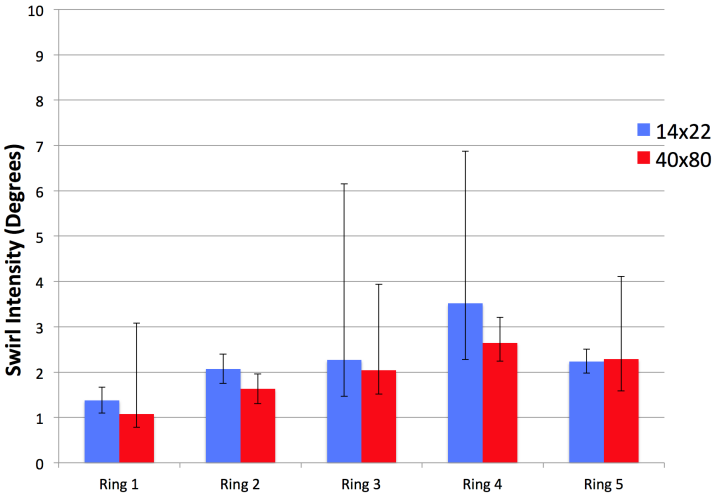

Figure 31: Swirl intensity beta -30°, Mach 0.065, alpha 1°.

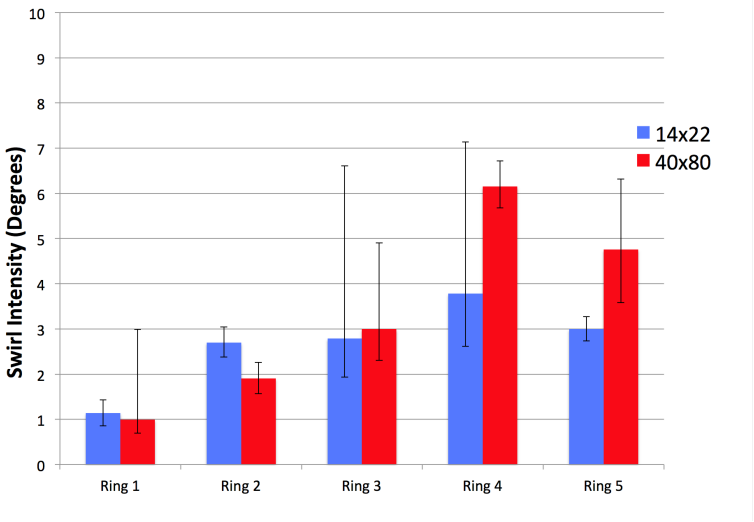

Figure 32: Swirl intensity beta -40°, Mach 0.065, alpha 1°.

VII. Concluding Remarks

Two successful tests of an HWB with jet engine simulation ejectors were conducted at the NASA Langley 14- by 22-foot tunnel and the NASA Ames 40- by 80-foot tunnel. Data were collected to characterize the inflow conditions for engine operability analysis. Mass flow sweeps showed a small vortex being ingested during spool up although distortion levels remained within acceptable limits. Tunnel to tunnel comparisons of the data further confirmed the quality of the results. The CFD studies conducted to compare to experimental data showed excellent agreement for the angle of attacks examined, although failed to match the experimental data for the lower speed beta sweep. Finally, swirl data were obtained, however, was not easily analyzed both due to uncertainty in the data from missing ports and the lack of established published acceptable swirl conditions for engines. Overall, the test results included in this paper show that the distortion and pressure recovery levels were acceptable for engine operability.

Acknowledgments

The research reported in this paper was sponsored by the NASA Integrated Aviation Systems Research Program Environmentally Responsible Aviation Project. The authors would like to thank the test teams at both NASA Langely's 14- by 22-foot tunnel and NASA Ames's 40- by 80-foot tunnel. In particular the contributions of Kurtis Long and Christina Ngo for all their work on the swirl rake both before and during the test.

References

[1] "NASA Aeronautics Strategic Implementation Plan," NP-2015-03-1479-HQ, 2015.

[2] Nicol, C. L. and Haller, W. J., "Assessment of the Fuel Burn Reduction Potential of Advanced Subsonic Transport Concepts for NASA's Environmentally Responsible Aviation Project," AIAA Paper, 54th AIAA Aerospace Sciences Mtg., 4–8 January 2016, (submitted for publication).

[3] Vicroy, D. D., Dickey, E. D., Princen, N. H., and Beyar, M. D., "Overview of Low-speed Aerodynamic Tests on a 5.75Blended-Wing-Body Twin Jet Configuration," AIAA Paper, 54th AIAA Aerospace Sciences Mtg., 4–8 January 2016, (submitted for publication).

[4] Long, K. R., Shea, P. R., Flamm, J. D., Schuh, M., James, K. D., Sexton, M. R., Tomkins, D. M., and Beyar, M. D., "Turbine Power Simulator Calibration and Testing for Hybrid Wing Body Powered Airframe Integration," AIAA Paper, 54th AIAA Aerospace Sciences Mtg., 4–8 January 2016, (submitted for publication).

[5] Garica, J. A., Melton, J. E., Schuh, M., James, K. D., Deere, K. A., Luckring, J. M., Carter, M. B., Vicroy, D. D., Flamm, J. D., Stremel, P. M., Nikaido, B. E., Childs, R. E., and Long, K. R., "NASA ERA Integrated CFD for Wind Tunnel Testing of Hybrid Wing-Body Configuration," AIAA Paper, 54th AIAA Aerospace Sciences Mtg., 4–8 January 2016, (submitted for publication).

[6]Gentry, G. L. J., Quinto, P. F., Gatlin, G. M., and Applin, Z. T., "The Langley 14- by 22-Foot Subsonic Tunnel: Description, Flow Characteristics and Guide for Users," NASA Technical Paper 3008, 1990.

[7]Hunt, R. and Sacco, J., "Activation and Operation of the National Full-Scale Aerodynamics Complex," AIAA Paper 2000-1076, 38th Aerospace Sciences Mtg., 10–13 January 2000, Reno, NV.

[8]Soderman, P. T., Jaeger, S. M., Hayes, J. A., and Allen, C. S., "Acoustic Quality of the 40- by 80-Foot Wind Tunnel Test Section After Installation of a Deep Acoustic Lining," NASA Technical Publication 2002-211851.

[9]Dickey, E. D., Princen, N. H., Bonet, J. T., and Ige, G. K., "Wind Tunnel Model Design and Fabrication of a 5.75Jet Configuration," AIAA Paper, 54th AIAA Aerospace Sciences Mtg., 4–8 January 2016, (submitted for publication).

[10]Carter, M. B., Shea, P. R., Flamm, J. D., Vicroy, D. D., Long, K. R., Kevin D. James, M. D. B., Tompkins, D. M., and Sexton, M. R., "Low-Speed Inlet Performance Characteristics of a 5.75-Percent Scale Blended Wing Body Twin Jet Configuration," NASA TM, 2016, (submitted for publication).

[11]Berrier, B. L. and Allan, B. G., "Experimental and Computational Evaluation of Flush-Mounted, S-Duct Inlets," AIAA Paper 2004-0764, 42nd AIAA Aerospace Sciences Mtg., 5–8 January 2004.

[12]"Inlet Total-Pressure-Distortion Considerations for Gas-Turbine Engines," SAE Aerospace Information Report 1419, 2013.

[13]Berrier, B. L., Carter, M. B., and Allan, B. G., "High Reynolds Number Investigation of a Flush-Mounted, S-Duct Inlet With Large Amounts of Boundary Layer Ingestion," NASA TP 2005-213766, September 1, 2005.

[14]"A Methodology for Assessing Inlet Swirl Distortion," October 2010, SAE Aerospace Information Report 5686.

[15]Taylor, J. R., *An Introduction to Error Analysis: The Study of Uncertainties in Physical Measurements*, University Science Books, 2nd ed., 1982.

[16]Tomkins, D. M., Sexton, M. M., Mugica, E. A., Beyer, M. D., Schuh, M., Stremel, P. M., Deere, K. A., McMillin, S. N., and Carter, M. B., "Computational Evaluation of Inlet Distortion on an Ejector Powered Hybrid Wing Body at Takeoff and Landing Conditions," AIAA Paper, 54th AIAA Aerospace Sciences Mtg., 4–8 January 2016, (submitted for publication).

[17]Chakravarthy, S., Peroomian, O., Goldberg, U., and Palaniswamy, S., "The CFD++ computational fluid dynamics software suite," AIAA Paper 1998-5564, 1998 World Aviation Conference, September, 1998.